SUPPORTING INFORMATION

Chinese Journal of Structural Chemistry

Strong High Entropy Alloy-Support Interaction Enables Efficient Electrocatalytic Water Splitting at High Current Density

Hongdong Li[1], Yue Pan[1], Jianping Lai[1]*, Lei Wang[1,2]* and Shouhua Feng[1]

[1]*Key Laboratory of Eco-chemical Engineering, Taishan Scholar Advantage and Characteristic Discipline Team of Eco-chemical Process and Technology, College of Chemistry and Molecular Engineering, Qingdao University of Science and Technology, Qingdao 266042, China*
[2]*Shandong Engineering Research Center for Marine Environment Corrosion and Safety Protection, College of Environment and Safety Engineering, Qingdao University of Science and Technology, Qingdao 266042, China*

**Corresponding authors. Emails: inorchemwl@126.com (L. Wang) and jplai@qust.edu.cn (J. Lai).*

n EXPERIMENTAL SECTION

Materials. Rhodium chloride hydrate ($RhCl_3$, 99.95%), ruthenium (III) chloride hydrate ($RuCl_3$, 99.95%), chloroplatinic acid hydrate (H_2PtCl_6, 99%), iridium (IV) chloride hydrate ($IrCl_4$, 99.9%) and potassium hydroxide (KOH, 90%) were bought from Aladdin. Iron (III) chloride hexahydrate ($FeCl_3$, 99%), nickel (II) chloride hexahydrate ($NiCl_2$, 99.95%), cobalt (II) chloride hexahydrate ($CoCl_2$, 98%) and copper (II) chloride dehydrate ($CuCl_2$, 99%) were bought from Alfa Aesar. Ethanol was supplied by Sinopharm Chemical Reagent Co., Ltd. Hydrophilic carbon cloth (CC, HCP330N) was bought from Shanghai Hesen Electric Co., Ltd. All reagents were used without further purification, and the electrolyte was freshly prepared with ultrapure water (18.2 MΩ cm^{-1}).

Preparation of HEA-NPs/CC. For the synthesis of PtRhCoNiCu HEA-NPs, the metal salt (H_2PtCl_6, $RhCl_3$, $CoCl_2$, $NiCl_2$, and $CuCl_2$) was dissolved in 1 mL of ethanol by sonication to prepare the mixed precursor (0.01 mol L^{-1} for each metal element).[1] The mixed solutions were directly dropped onto the carbon cloth with a loading of ~100 μL cm^{-2}. The precursor/CC was dried at room temperature and then sealed in a glass bottle filled with argon. The glass bottle was then transferred in the microwave oven (1000 W) for the microwave heating treatment. The heating time of the microwave oven was set as 10 s for a piece of precursor/CC. The synthesis of other HEA-NPs (PtRuCoNiCu, PtIrCoNiCu, RuRhCoNiCu, IrRhCoNiCu, IrRuCoNiCu, PtFeCoNiCu, RuFeCoNiCu, RhFeCoNiCu, and IrFeCoNiCu) on the CC was similar, only changing the type of metal salt. By ICP testing, the total metal loading of different materials is about: PtRhCoNiCu/CC (~0.41 mg cm^{-1}), PtRuCoNiCu/CC (~0.42 mg cm^{-1}), PtIrCoNiCu/CC (~0.45 mg cm^{-1}), PtFeCoNiCu/CC (~0.37 mg cm^{-1}), RuRhCoNiCu/CC (~0.34 mg cm^{-1}), RhFeCoNiCu/CC (~0.30 mg cm^{-1}), IrRhCoNiCu/CC (~0.40 mg cm^{-1}), IrRuCoNiCu/CC (~0.41 mg cm^{-1}), RuFeCoNiCu/CC (~0.29 mg cm^{-1}) and IrFeCoNiCu/CC (~0.36 mg cm^{-1}). To better verify whether HEA-NPs/CC is more active than Pt alone, we prepared the Pt/CC and PtRh/CC by the same method (the same total metal loading with PtRhCoNiCu/CC).

Preparation of HEA-NPs on CC. Typically, $Pt(acac)_2$, $Rh(acac)_3$, $Ni(acac)_2$, $Co(acac)_3$ and $Cu(acac)_2$ with equal molar ratio and $Mo(CO)_6$ were added to oleamine, kept at 200 °C for 2 h. After centrifugation, organic matter was removed with acetic acid. 4 mg PtRhCoNiCu catalyst powder was dispersed in 1.00 mL of mixed solution containing 0.74 mL of ethanol, 0.24 mL of water and 0.02 mL of 5 wt.% of Nafion solution, and the mixed solution was sonicated for 30 min to obtain highly dispersed suspensions. Then, 50 μL of the catalyst ink was dropped on a piece of clean CC substrate (coating area of 0.5 × 1 cm^2). After drying in vacuum at 60 °C, the loading amount of PtRhCoNiCu catalyst was about 0.40 mg cm^{-2}.

Characterization. The material morphology was examined by scanning electron microscope (SEM, Regulus8100) operating at 5 kV and the transmission electron microscopy (TEM) and high-resolution TEM (HRTEM) (FEI Tecnai-G2 F30 at an accelerating voltage of 300 KV). Powder X-ray diffraction (XRD) spectra were recorded on X'Pert-PRO MPD diffractometer operating at 40 kV and 40 mA with Cu Kα radiation. The X-ray photoelectron spectra (XPS) analyses were carried out with Axis Supra spectrometer using a monochromatic Al Kα source (15 mA, 14 kV). The compositions and metal loading of the HEA NPs on CC were determined by the inductively coupled plasma atomic emission spectrometer (ICP-AES, Varian 710-ES).

Electrochemical Measurements. Electrochemical measurements were performed on a Gamry Reference 600 Instrument with three-electrode setup. The graphite rod electrode as the counter electrode and a saturated calomel electrode (SCE) as the reference electrode. The as-prepared electrodes (HEA-NPs/CC) were utilized as the working electrode (working area: 0.5 cm^2). All the potentials reported in this work were converted to the reversible hydrogen electrode (RHE). The HER and OER performances of the catalysts were evaluated by linear sweep voltammetry (LSV) with a scan rate of 5 mV s^{-1} in N_2-saturated (HER) or O_2-saturated (OER) 1.0 M KOH solution, and all polarization curves were 95% iR-corrected. Commercial Pt/C and RuO_2 were also used as control samples, and the loading amount of 20 wt.% Pt/C or RuO_2 catalyst was about 1.00 and 0.40 mg cm^{-2}. EIS was tested by the three-electrode system from 100,000 to 0.01 Hz; the test potential was -0.05 and 1.50 V *vs.* RHE for HER and OER (the amplitude is 5 mV). The durability tests were performed in 1.0 M KOH solution using the chronopotentiometry method and 10,000 cycles. The electrical double-layer capacitance (C_{dl}) was measured from CV measurements in a small potential range of 0.86-1.06 V *vs.* RHE with scan rate from 20 to 100 mV s^{-1}. The value of linear slope is the C_{dl} used to represent ECSA.

Calculation of turnover frequency (TOF): The TOF value was calculated as follows

$$\mathrm{TOF}(S^{-1}) = \frac{js}{2*F*n} \qquad \text{HER}$$

$$\mathrm{TOF}(S^{-1}) = \frac{js}{4*F*n} \qquad \text{OER}$$

Where *j* is the measured current density (A cm^{-2}), *S* is the geometric area of working electrode (cm^2), *n* is the moles of active materials deposited on the working electrode (n is based on the moles of all metal species), the number 2 or 4 represents two or four electrons (produce one hydrogen or oxygen molecule), and *F* is the Faradic constant (96485 C mol^{-1}). In this case, the calculated value is a lower limit of TOF.

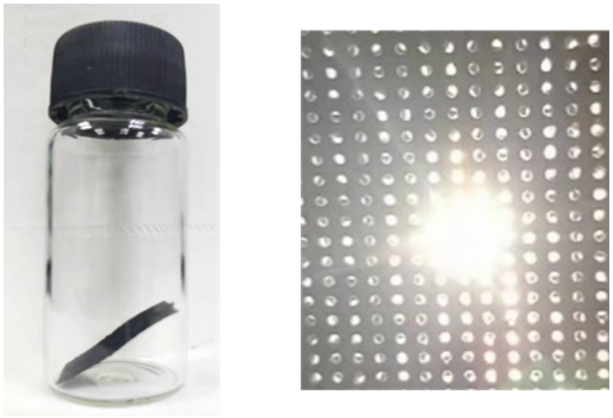

Figure S1. The photograph of CC sample in a vial container before being put into a microwave oven (left). The photograph showing the sample during flash ignition (right).

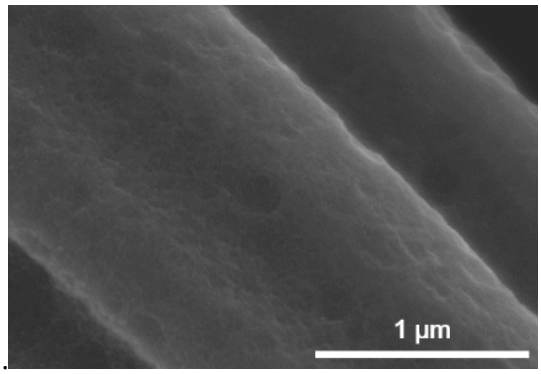

Figure S2. SEM image of CC after microwave heating.

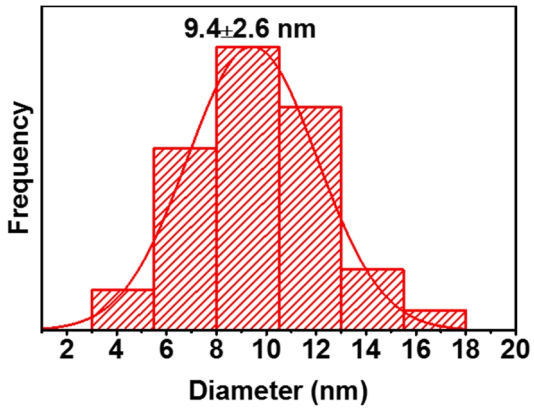

Figure S3. The histogram of the diameter of PtRhCoNiCu/CC.

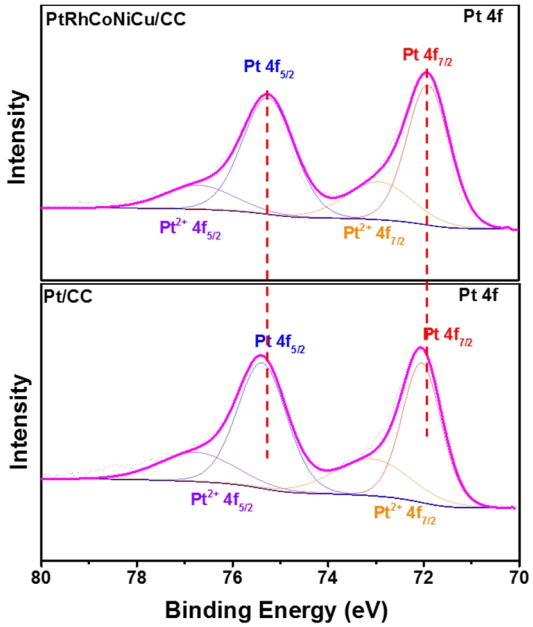

Figure S4. Pt 4f XPS spectrum of PtRhCoNiCu/CC and Pt/CC.

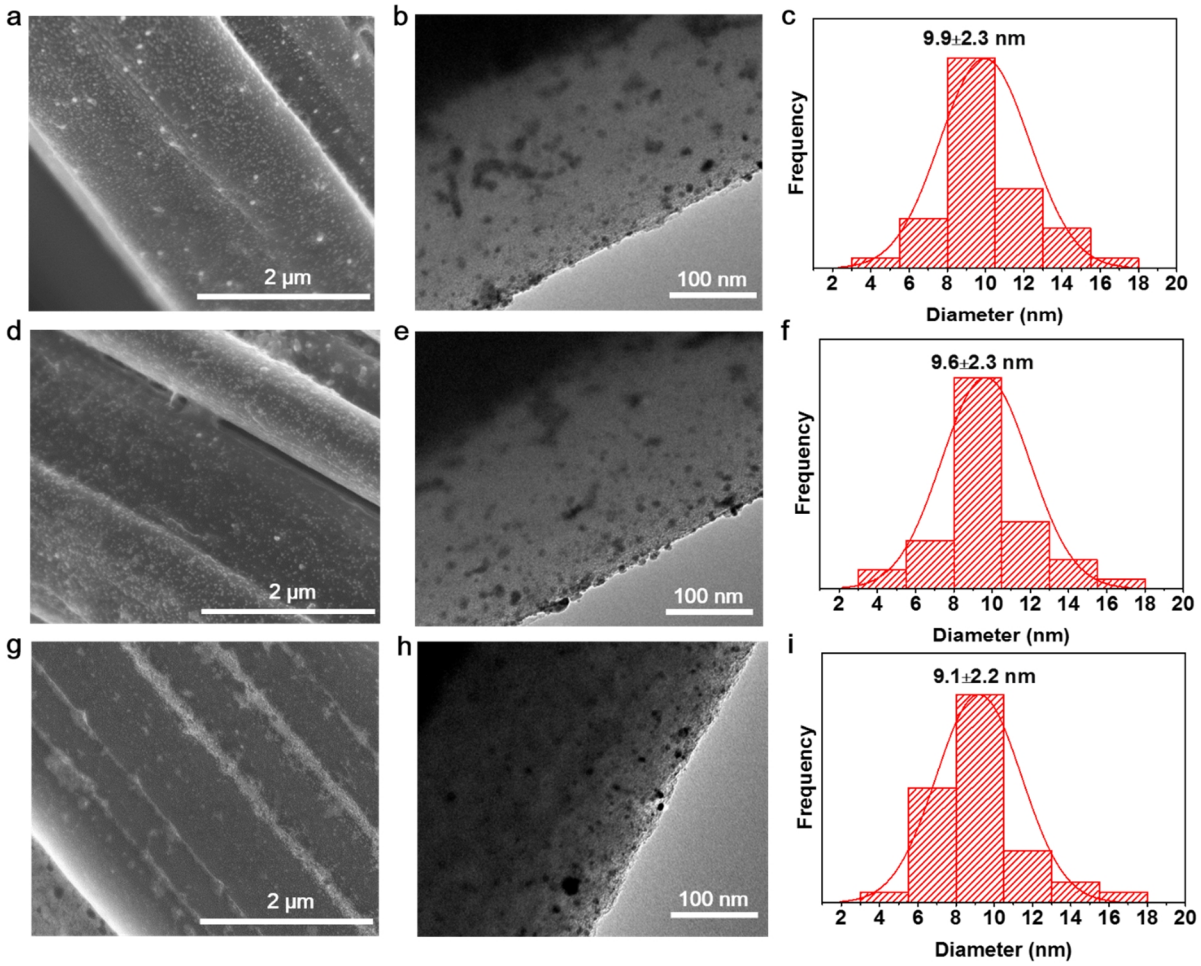

Figure S5. SEM images of (a) PtIrCoNiCu/CC, (d) PtRuCoNiCu/CC and (g) PtFeCoNiCu/CC. TEM images of (b) PtIrCoNiCu/CC, (e) PtRuCoNiCu/CC and (h) PtFeCoNiCu/CC. The histograms of the diameter of (c) PtIrCoNiCu/CC, (f) PtRuCoNiCu/CC and (i) PtFeCoNiCu/CC.

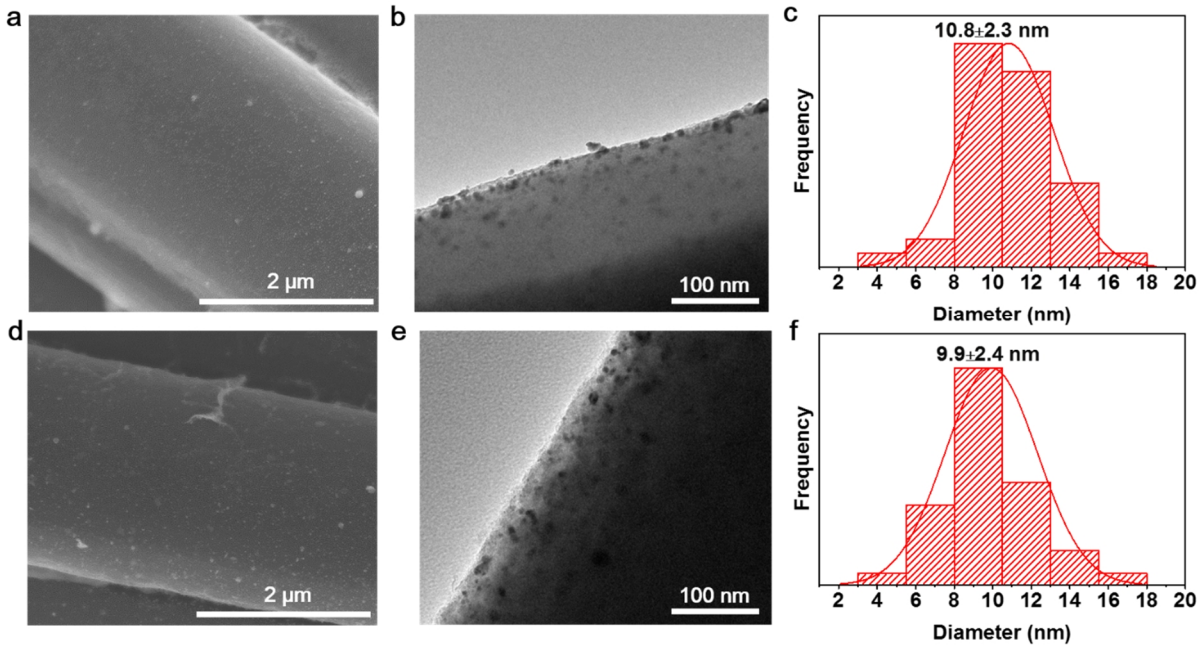

Figure S6. SEM images of (a) IrRhCoNiCu/CC and (d) RuRhCoNiCu/CC. TEM images of (b) IrRhCoNiCu/CC and (e) RuRhCoNiCu/CC. The histograms of the diameter of (c) IrRhCoNiCu/CC and (f) RuRhCoNiCu/CC.

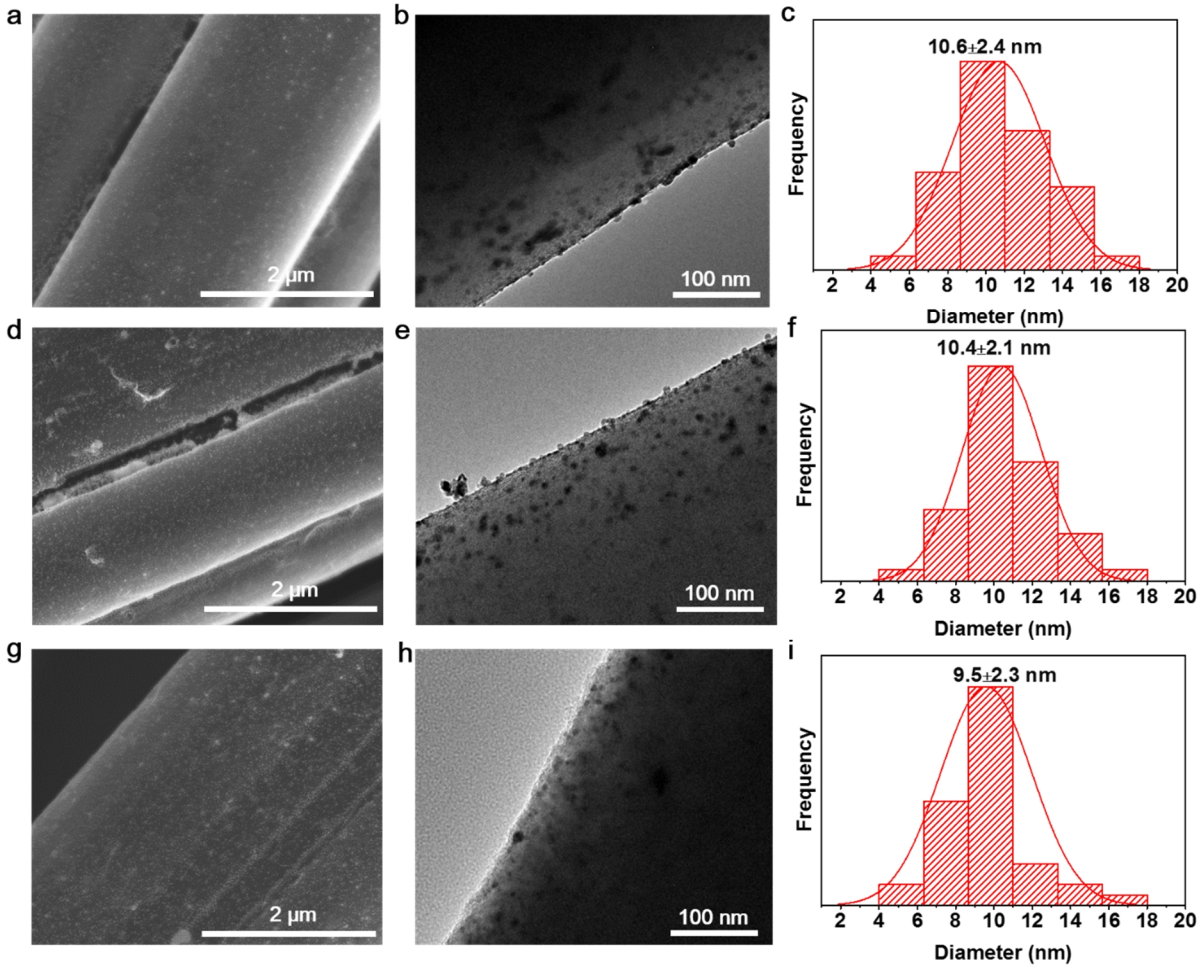

Figure S7. SEM images of (a) IrFeCoNiCu/CC, (d) RhFeCoNiCu/CC and (g) RuFeCoNiCu/CC. TEM images of (b) IrFeCoNiCu/CC, (e) RhFeCoNiCu/CC and (h) RuFeCoNiCu/CC. The histograms of the diameter of (c) IrFeCoNiCu/CC, (f) RhFeCoNiCu/CC and (i) RuFeCoNiCu/CC.

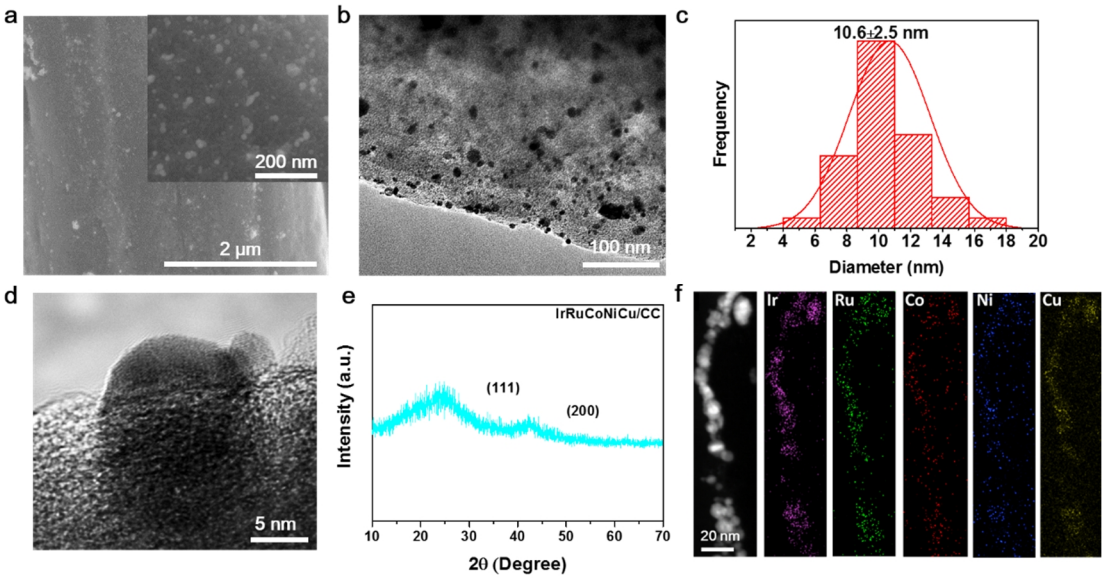

Figure S8. (a) SEM, (b) TEM, (c) The histograms of the diameter, (d) HRTEM images, (e) XRD and (f) EDX elemental mappings of Ir, Ru, Co, Ni, and Cu of IrRuCoNiCu/CC.

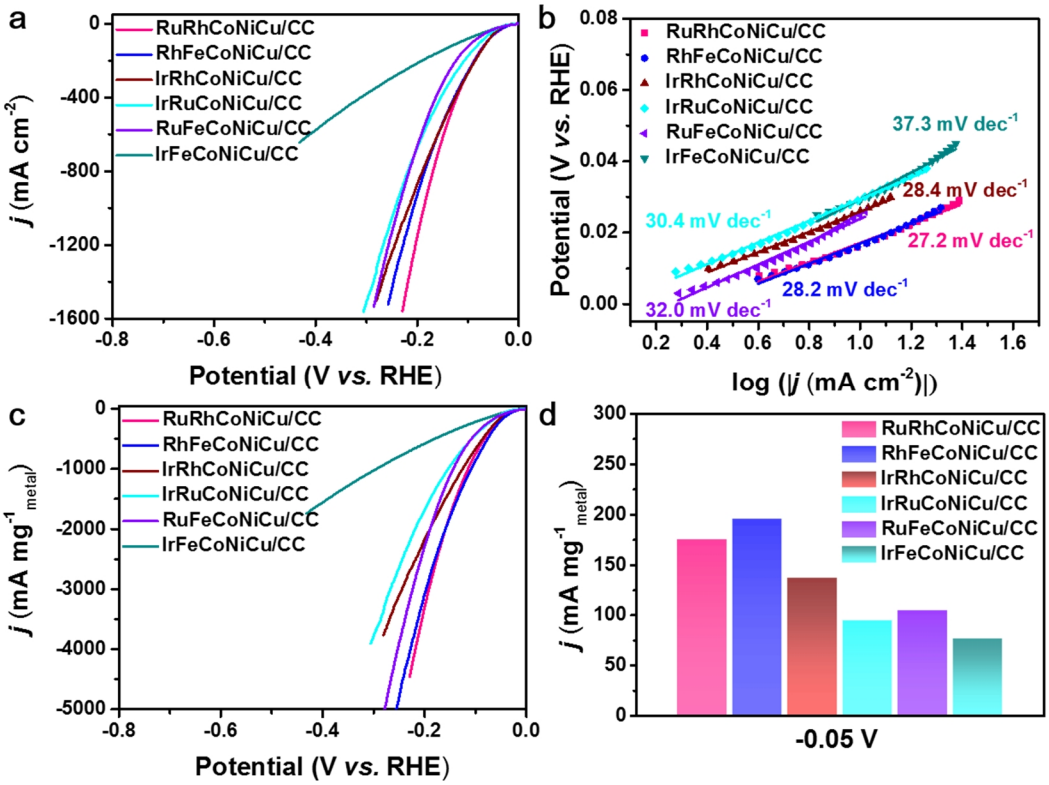

Figure S9. (a) LSV curves, (e) Tafel curves, (c) mass activity of LSV curves, (d) the mass activities at the potential of -0.05 V *vs.* RHE of HEA-NPs/CC for HER.

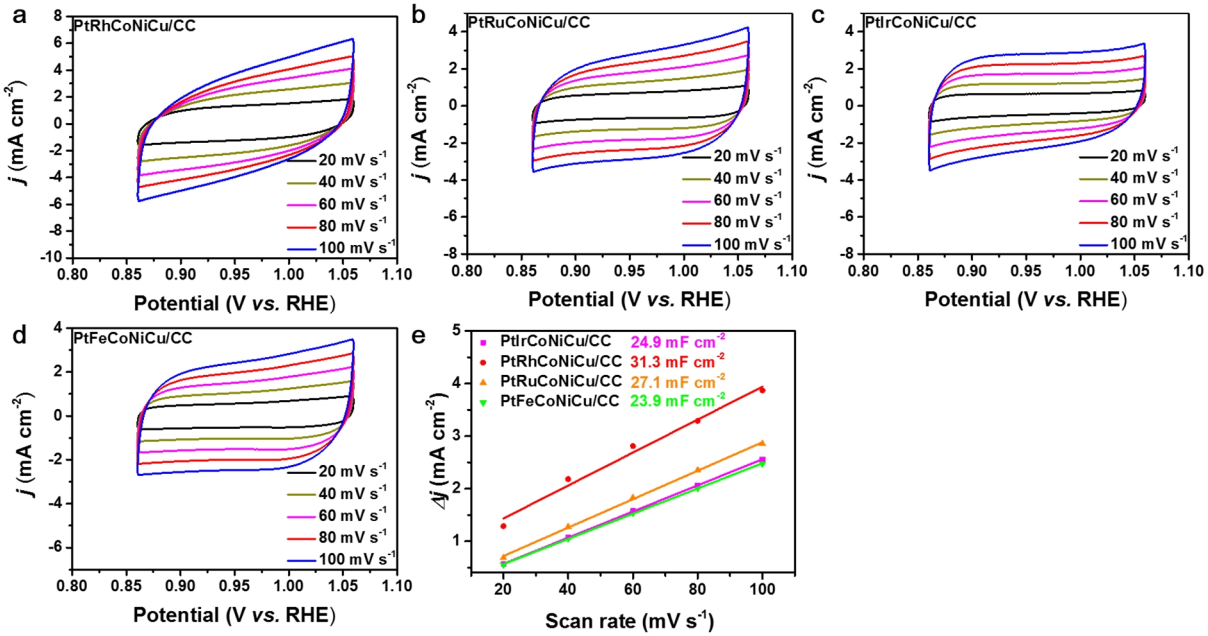

Figure S10. (a-d) Typical CVs of the samples with scan rates ranging from 20 to 100 mV s^{-1}; (e) Estimation of C_{dl} by plotting the capacitive current density against the scan rate to fit a linear regression.

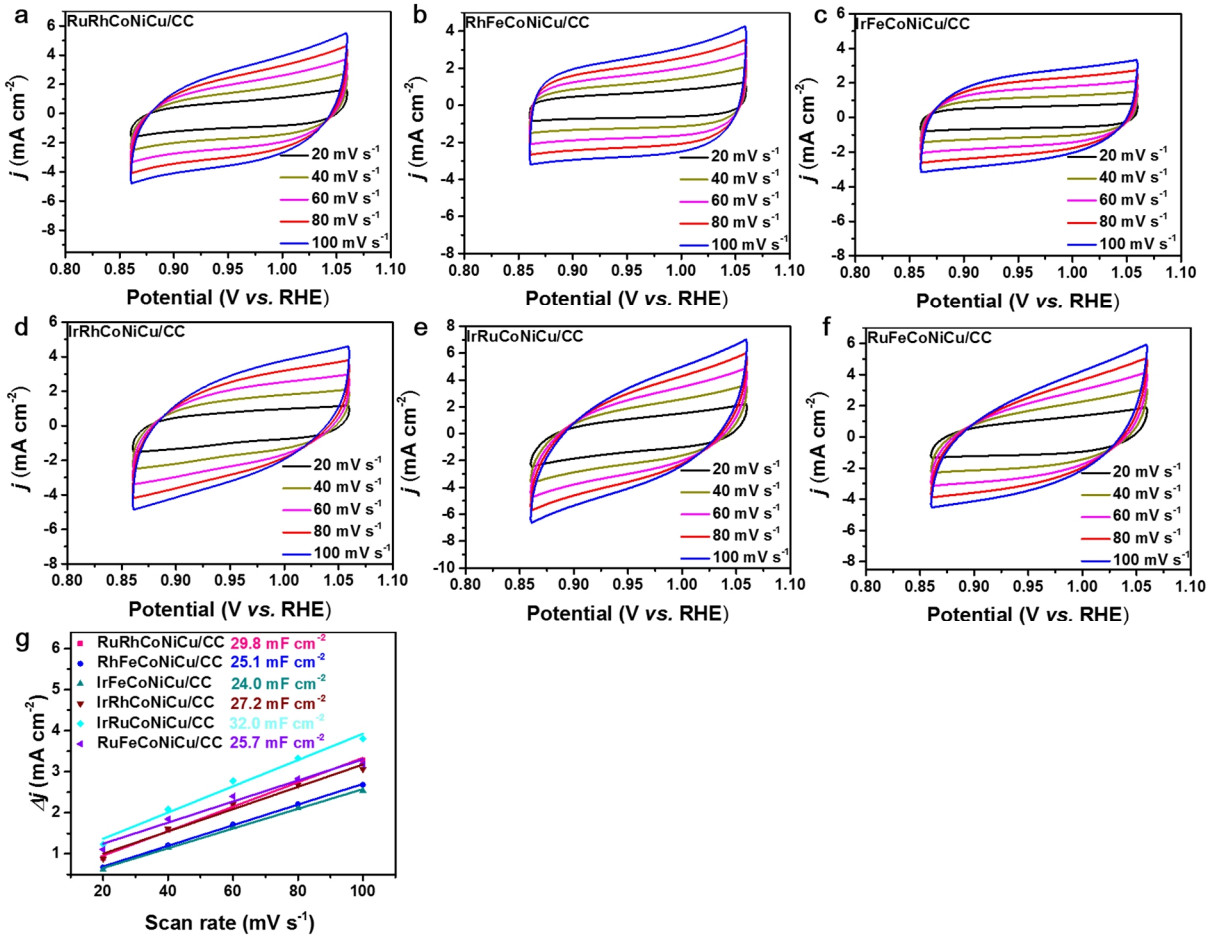

Figure S11. (a-f) Typical CVs of the samples with scan rates ranging from 20 to 100 mV s^{-1}; (g) Estimation of C_{dl} by plotting the capacitive current density against the scan rate to fit a linear regression.

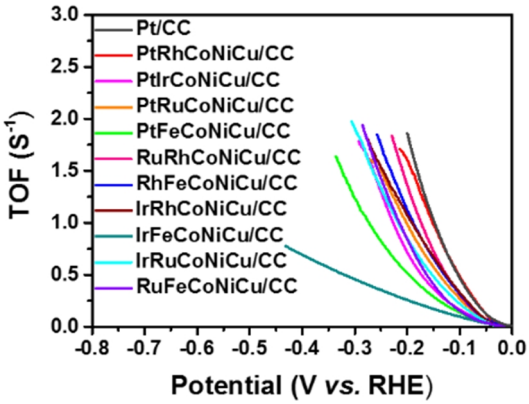

Figure S12. TOF values of different samples for HER.

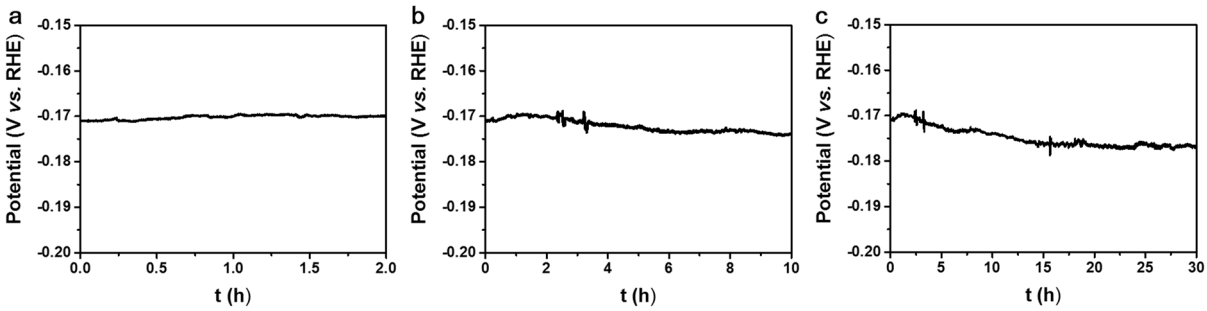

Figure S13. CP curve of PtRhCoNiCu/CC at -1000 mA cm^{-2} with different times.

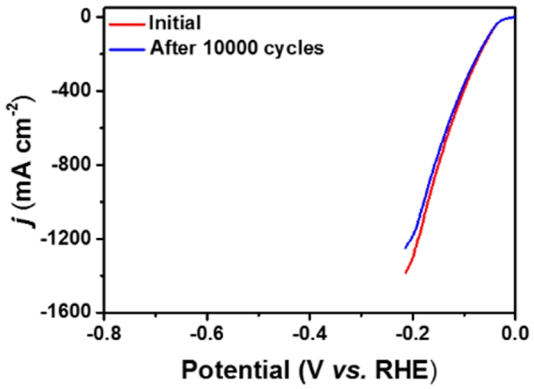

Figure S14. LSV curves of PtRhCoNiCu/CC before and after 10,000 cycles in HER.

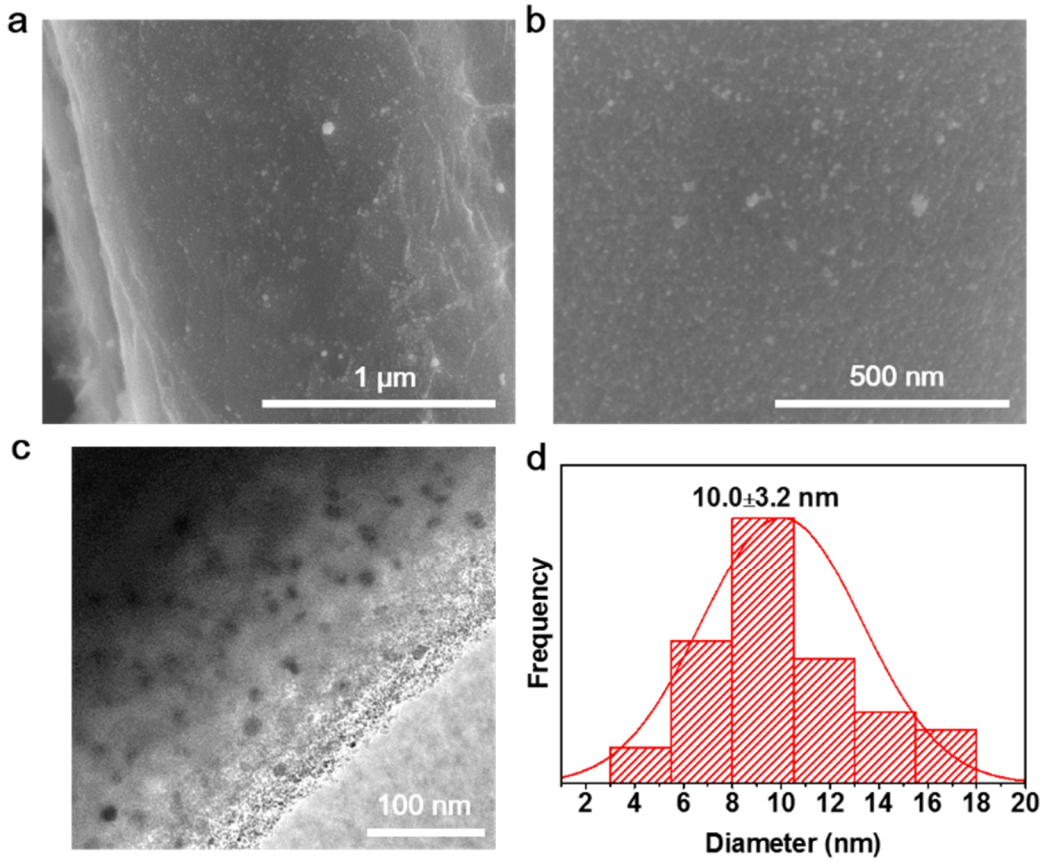

Figure S15. (a) and (b) SEM and (c) TEM images, (d) The histogram of the diameter of PtRhCoNiCu/CC after HER stability test.

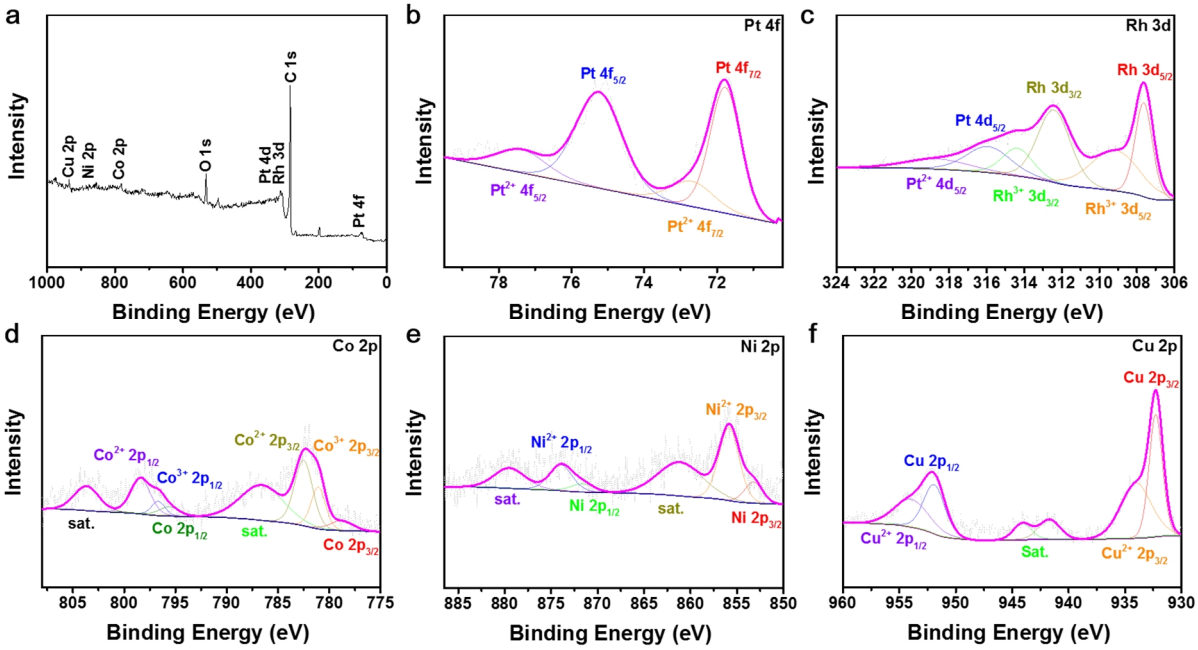

Figure S16. XPS compositional analysis of PtRhCoNiCu/CC sample after HER stability test. (a) XPS survey spectrum. (b) Pt 4f XPS spectrum. (c) Rh 3d XPS spectrum. (d) Co 2p XPS spectrum. (e) Ni 2p XPS spectrum. (f) Cu 2p XPS spectrum.

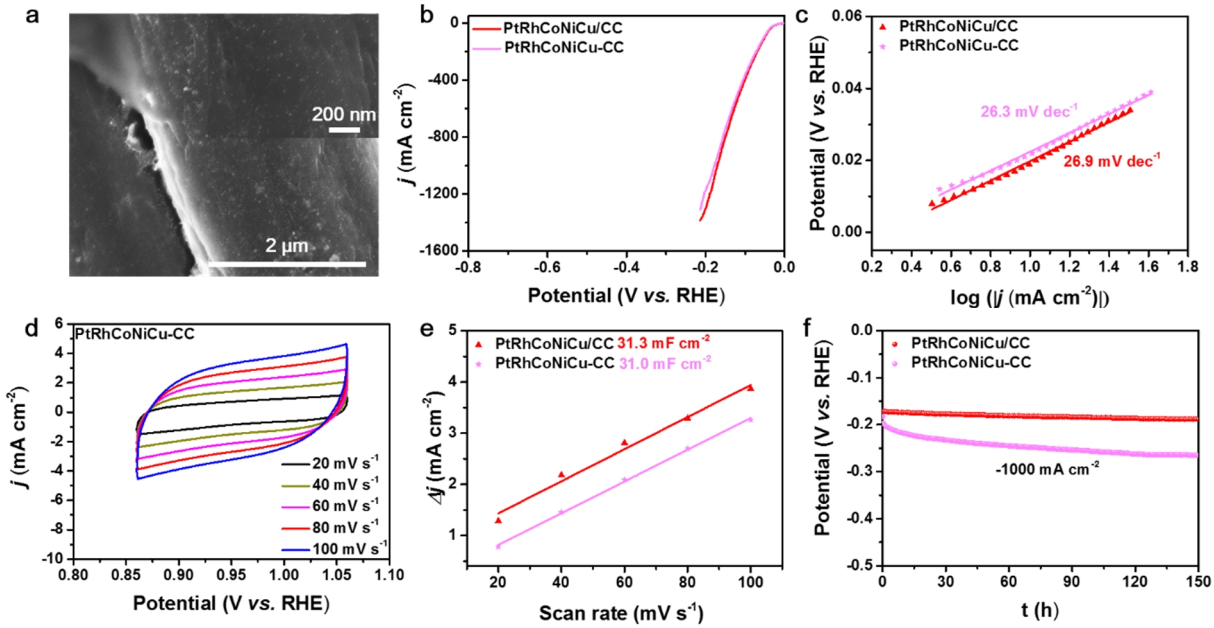

Figure S17. (a) The SEM images of PtRhCoNiCu-CC. (b) LSV curves, (c) Tafel curves of PtRhCoNiCu/CC and PtRhCoNiCu-CC for HER. (d) Typical CVs of the samples with scan rates ranging from 20 to 100 mV s^{-1} of PtRhCoNiCu-CC. (e) Cdl curves, (f) CP curves of PtRhCoNiCu/CC and PtRhCoNiCu-CC for HER.

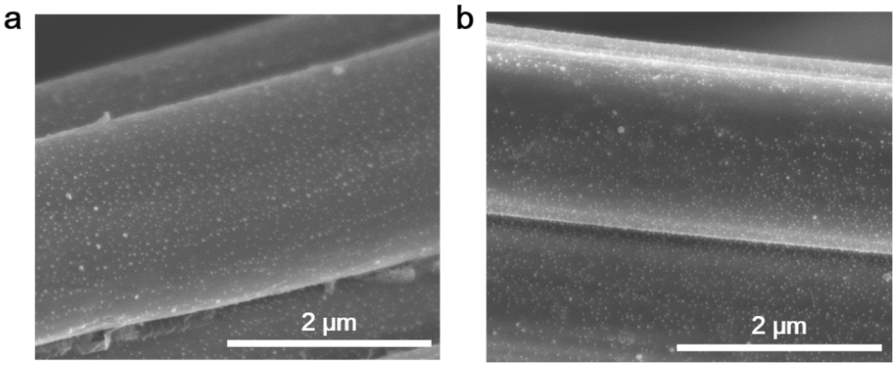

Figure S18. The SEM images of (a) Pt/CC and (b) PtRh/CC.

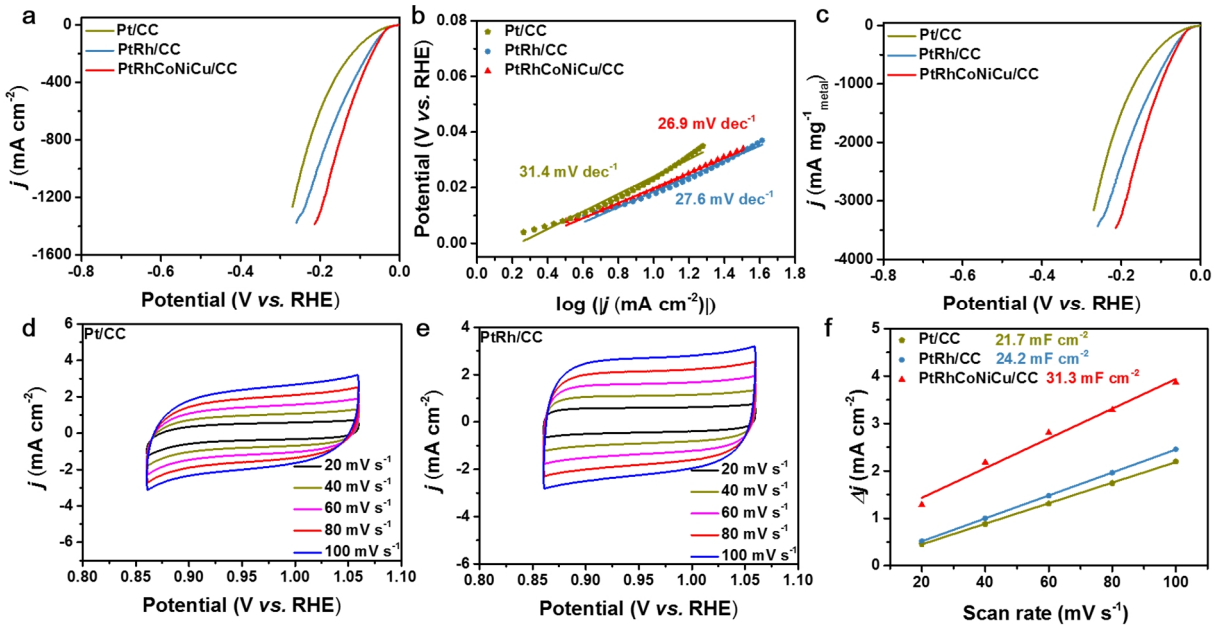

Figure S19. (a) LSV curves, (b) Tafel curves, (c) mass activity of LSV curves of Pt/CC, PtRh/CC and PtRhCoNiCu-CC for HER. Typical CVs of the samples with scan rates ranging from 20 to 100 mV s^{-1} of (d) Pt/CC and (e) PtRh/CC. (f) Cdl curves of Pt/CC, PtRh/CC and PtRhCoNiCu/CC.

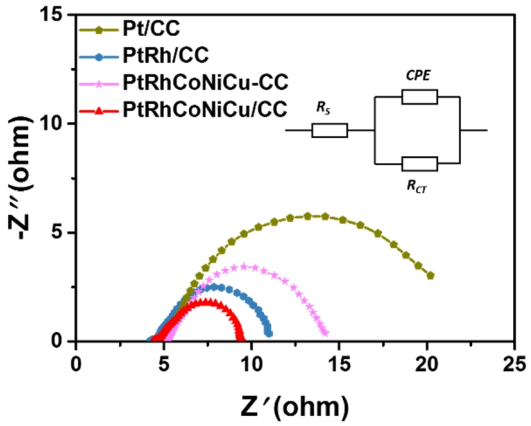

Figure S20. The EIS curves of Pt/CC, PtRh/CC, PtRhCoNiCu-CC and PtRhCoNiCu/CC in HER.

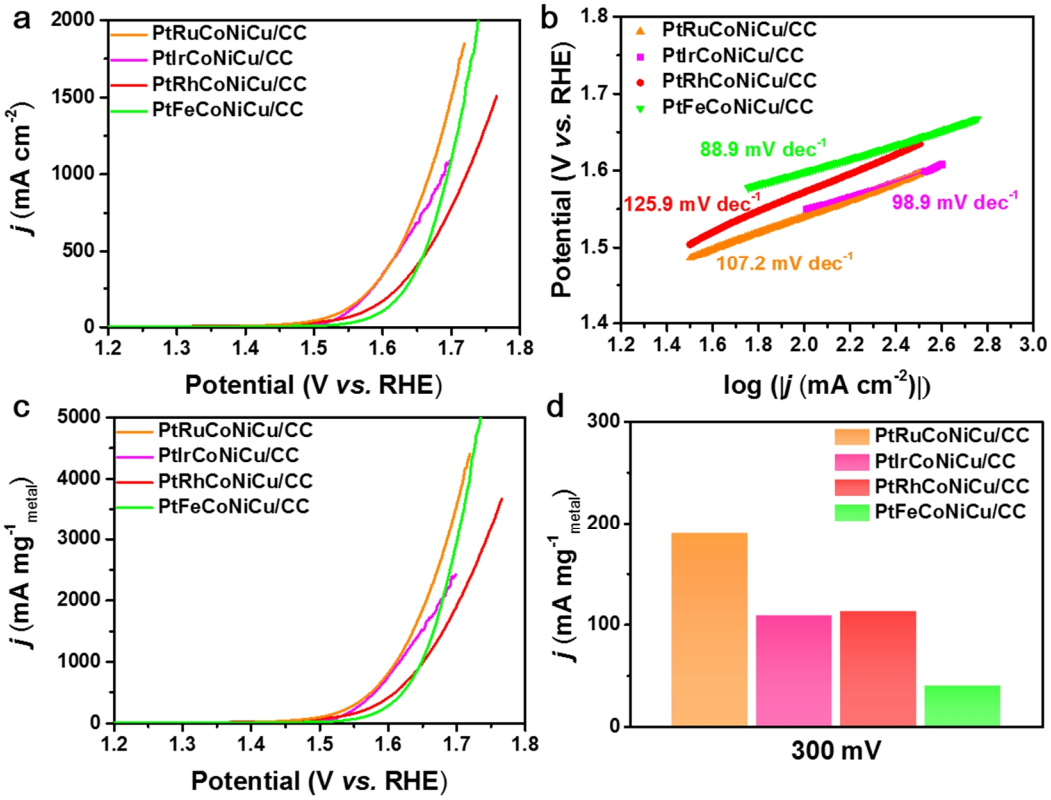

Figure S21. (a) LSV curves, (e) Tafel curves, (c) mass activity of LSV curves, (d) the mass activities at the overpotential of 300 mV of HEA-NPs/CC for OER.

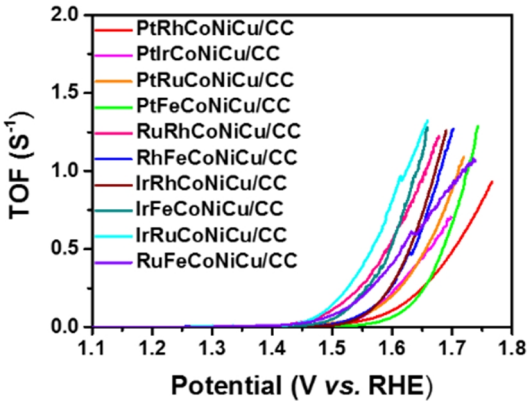

Figure S22. TOF values of HEA-NPs/CC samples for OER.

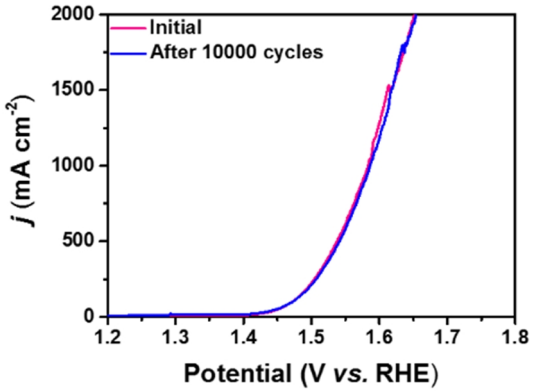

Figure S23. LSV curves of IrRuCoNiCu/CC before and after 10,000 cycles in OER.

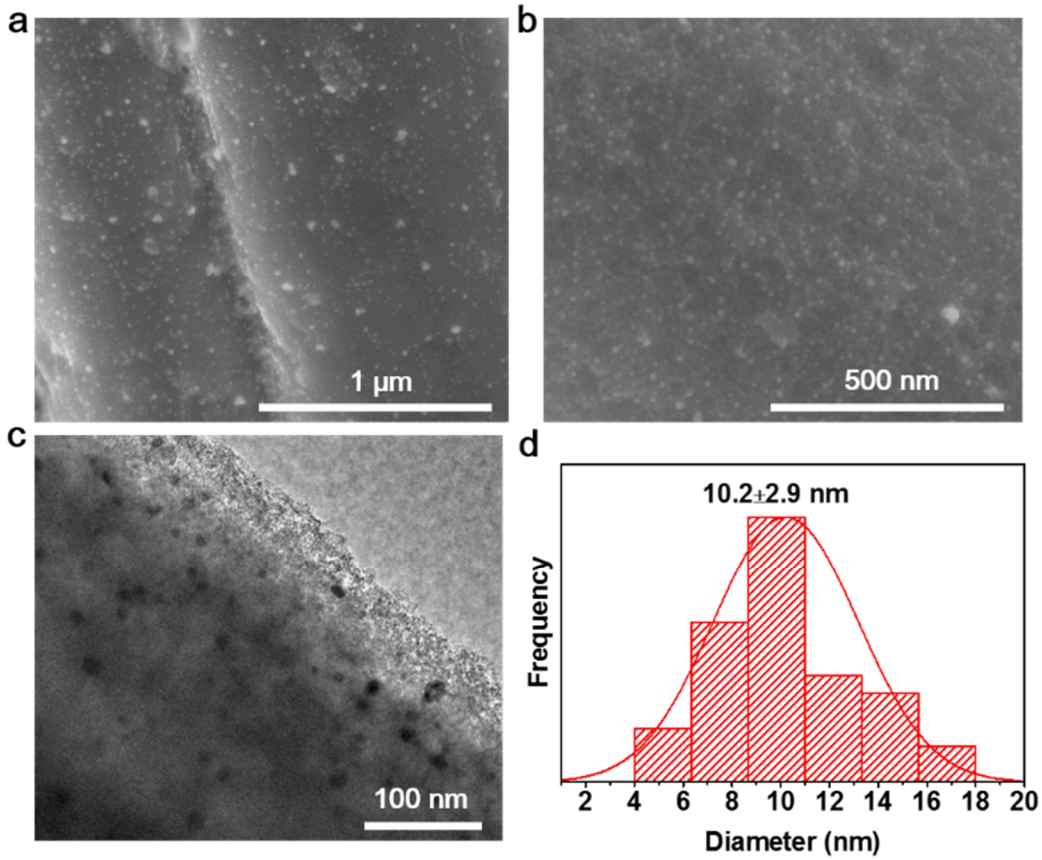

Figure S24. (a) and (b) SEM and (c) TEM images, (d) The histogram of the diameter of of IrRuCoNiCu/CC after OER stability test.

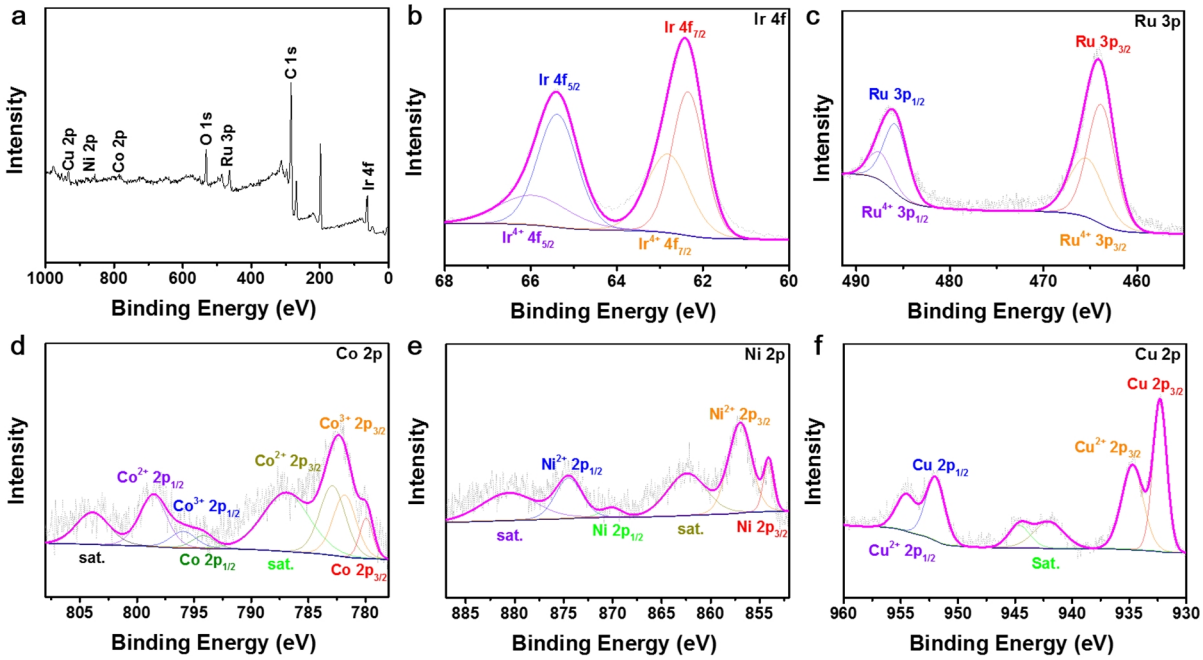

Figure S25. XPS compositional analysis of IrRuCoNiCu/CC sample before OER stability test. (a) XPS survey spectrum. (b) Ir 4f XPS spectrum. (c) Ru 3p XPS spectrum. (d) Co 2p XPS spectrum. (e) Ni 2p XPS spectrum. (f) Cu 2p XPS spectrum.

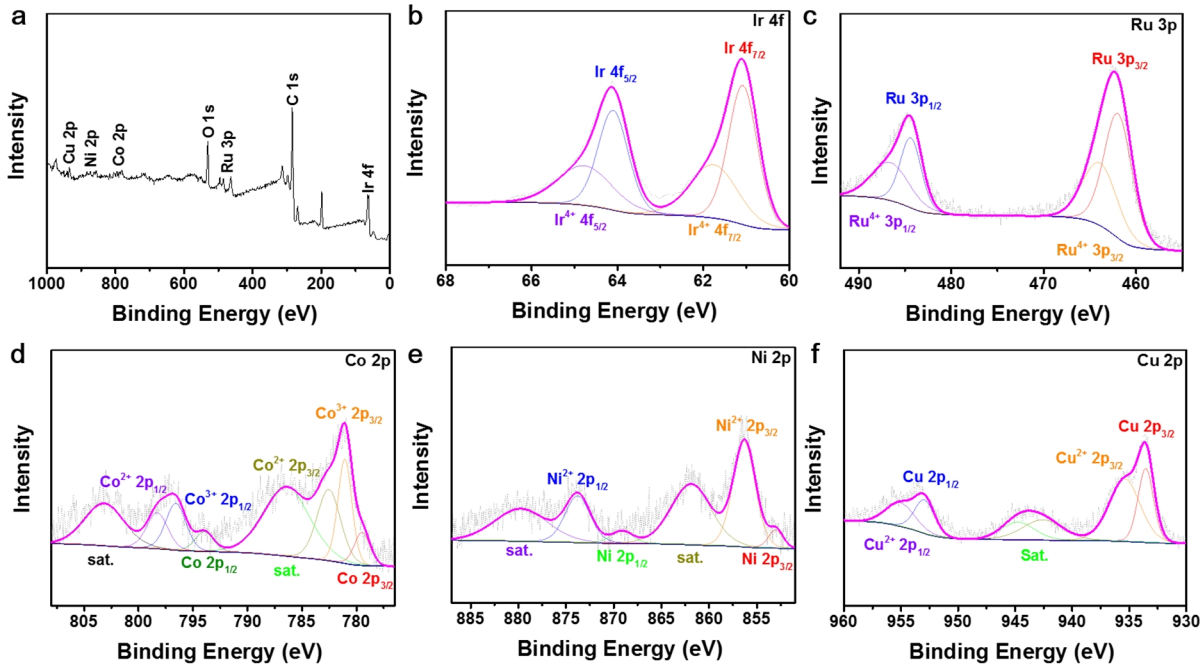

Figure S26. XPS compositional analysis of IrRuCoNiCu/CC sample after OER stability test. (a) XPS survey spectrum. (b) Ir 4f XPS spectrum. (c) Ru 3p XPS spectrum. (d) Co 2p XPS spectrum. (e) Ni 2p XPS spectrum. (f) Cu 2p XPS spectrum.

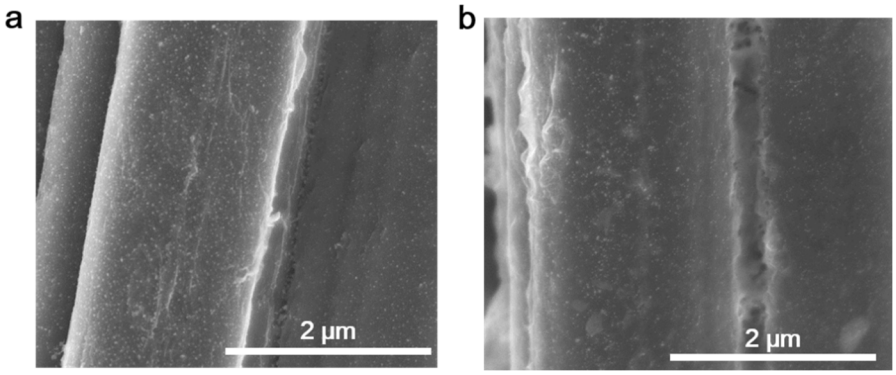

Figure S27. The SEM images of (a) Ru/CC and (b) IrRu/CC.

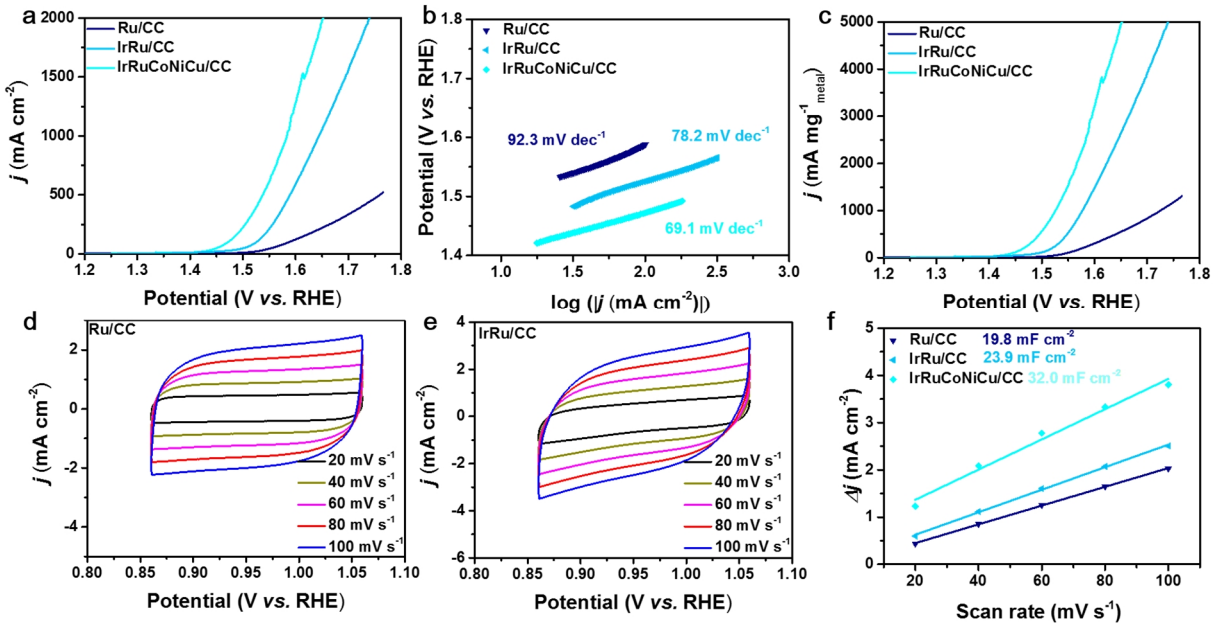

Figure S28. (a) LSV curves, (b) Tafel curves, (c) mass activity of LSV curves of Ru/CC, IrRu/CC and IrRuCoNiCu-CC for HER. Typical CVs of the samples with scan rates ranging from 20 to 100 mV s^{-1} of (d) Ru/CC and (e) IrRu/CC. (f) Cdl curves of Ru/CC, IrRu/CC and IrRuCoNiCu/CC.

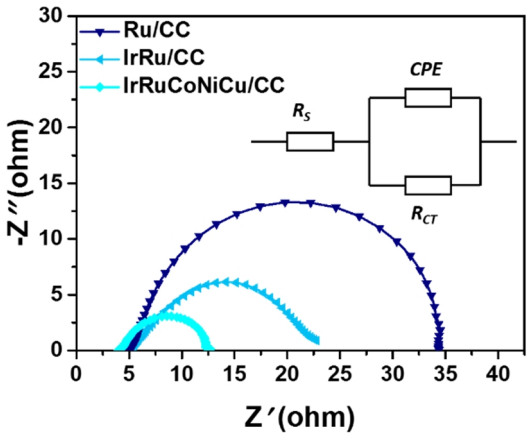

Figure S29. The EIS curves of Ru/CC, IrRu/CC and IrRuCoNiCu/CC in OER.

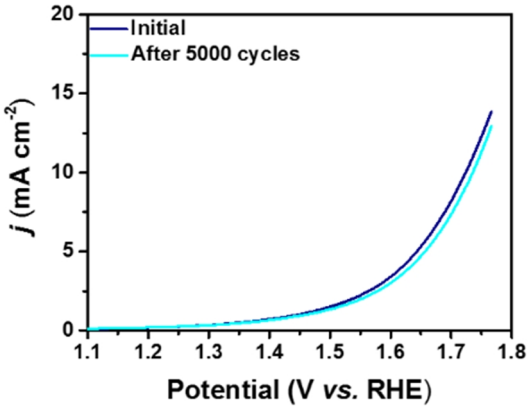

Figure S30. LSV curves of CC before and after 5,000 cycles in OER.

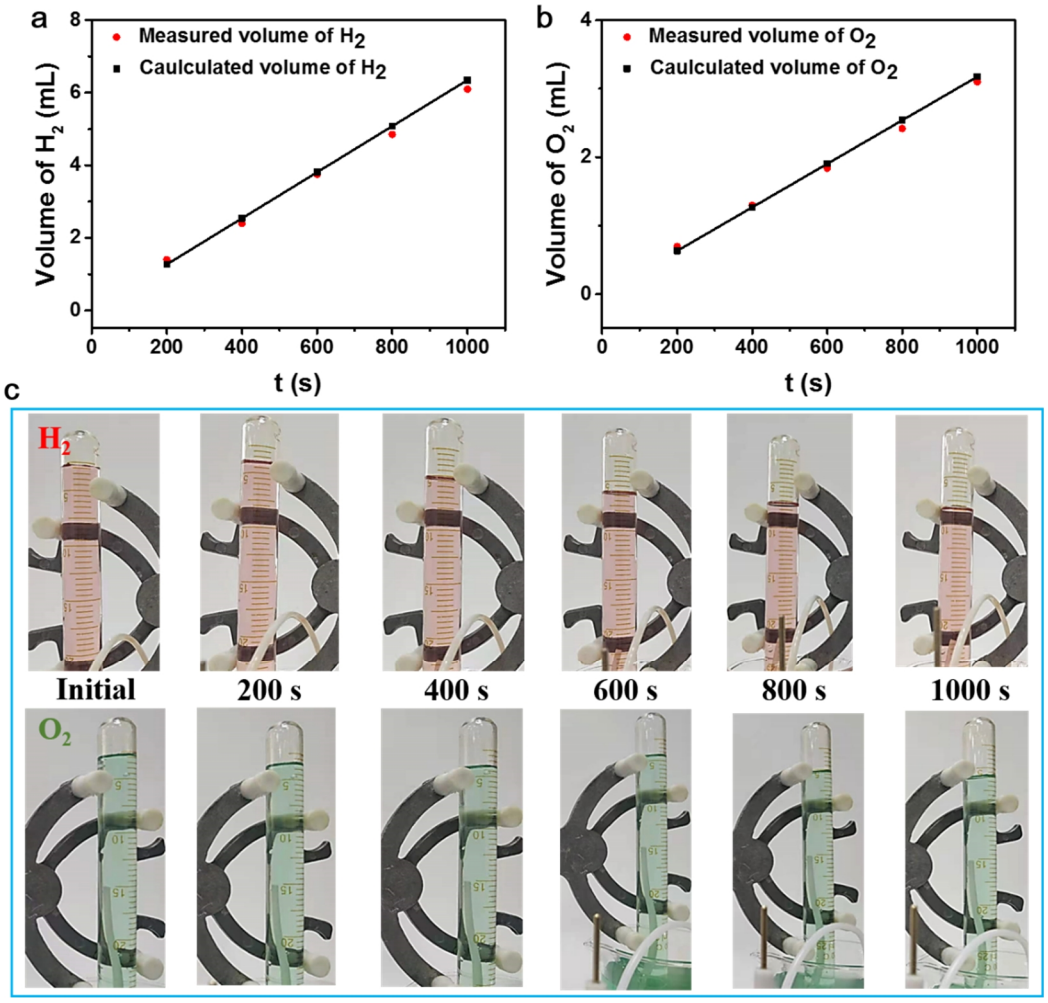

Figure S31. (a, b) Volume of H_2 and O_2 actually measured at 50.0 mA versus time for PtRhCoiNiCu/CC//IrRuCoNiCu/CC in 1.0 M KOH solution; (c) volume of H_2 and O_2 at 0, 200, 400, 600, 800, and 1000 s.

Table S1. Elemental Ratio in HEA-NPs

Samples	Pt Atomic ratio	Rh Atomic ratio	Ru Atomic ratio	Ir Atomic ratio	Co Atomic ratio	Ni Atomic ratio	Cu Atomic ratio	Fe Atomic ratio
PtRhCoNiCu	32%	22%	-	-	11%	15%	20%	-
PtRuCoNiCu	33%	-	24%	-	12%	13%	18%	-
PtIrCoNiCu	32%	-	-	23%	14%	15%	16%	-
PtFeCoNiCu	30%	-	-	-	15%	17%	20%	18%
RuRhCoNiCu	-	25%	28%	-	13%	15%	19%	-
RhFeCoNiCu	-	28%	-	-	16%	21%	19%	16%
IrRhCoNiCu	-	25%	-	27%	11%	17%	20%	-
IrRuCoNiCu	-	-	23%	30%	14%	15%	18%	-
RuFeCoNiCu	-	-	28%	-	16%	20%	21%	15%
IrFeCoNiCu	-	-	-	31%	15%	18%	20%	16%

Table S2. Fitting Parameters of the EIS Results Based on the Equivalent Circuits

Samples	R_S	R_{CT}
PtRhCoNiCu/CC	4.835	5.297
PtRuCoNiCu-CC	5.119	9.345
PtRh/CC	4.866	6.929
Pt/CC	4.891	17.63
IrRuCoNiCu/CC	4.635	8.525
IrRu/CC	4.821	17.977
Ru/CC	5.065	30.561

Table S3. Comparison of HER Performance of Ptrhconicu and Recent Reported Electrocatalysts

Electrocatalyst	Substrate	J (mA cm^{-2})	η(mV)@J	Tafel (mV dec^{-1})	Ref.
PtRhCoNiCu	carbon cloth	-10 -100 -500 -1000	19 51 115 170	26.9	This work
$Ni_{20}Fe_{20}Mo_{10}Co_{35}Cr_{15}$	self-supporting electrode	-10	170	66	[2]
PtAuPdRhRu	glassy carbon	-30	190	62	[3]
FeCoPdIrPt NPs	carbon paper	-10	42	-	[4]
AlNiCoRuMo	glassy carbon	-10	24.5	30.3	[5]
IrPdPtRhRu	rotating disk electrode	-10	17.0	-	[6]
CuAlNiMoFe	self-supporting electrode	-10 -1840	9.7 240	60	[7]
PtNiFeCoCu/C	glassy carbon	-10	11	30	[8]
PdFeCoNiCu/C	glassy carbon	-10	18	39	[9]
Nanosponge PdPtCuNiP	self-supporting electrode	-10	32	37.4	[10]
$Fe_{10.06}Ni_{43.23}Co_{23.69}Al_{8.61}Ti_{14.41}$	self-supporting electrode	-10	88.2	40.1	[11]
(Ru-Co)Ox/CC	carbon cloth	-10 -100	44.1 89.1	23.5	[12]

Table S4. Comparison of OER Performance of IrRuCoNiCu and Recent Reported Electrocatalysts.

Electrocatalyst	Substrate	J (mA cm^{-2})	η(mV)@J	Tafel (mV dec^{-1})	Ref.
IrRuCoNiCu	carbon cloth	10 100 500 1000	166 242 308 354	69.1	This work
FeNiMnCrCu	self-supporting electrode	100	599	-	[13]
np-AlNiCoFeMo	glassy carbon	10	240	46	[14]
HEAN@NPC/CC-450	carbon fiber electrode	10	263	43	[15]
AlNiCoRuMo	glassy carbon	10	245	54.5	[5]
CoCrFeNiAl	glassy carbon	10	240	52.7	[16]
$Fe_{10.06}Ni_{43.23}Co_{23.69}Al_{8.61}Ti_{14.41}$	self-supporting electrode	10	299	37.9	[11]
$La(CrMnFeCo_2Ni)O_3$	Ni foam	10	325	51.2	[17]
FeNiCoCrMn-HEG	Ni foam	10	229	40	[18]
$FeNiCoCrMnS_2$	Ni foam	10 100 500 1000	199 246 285 308	39.1	[19]
CoFeLaNiPt HEMG-NP	-	10	377	-	[20]
(CrMnFeCoNi)Sx	-	100	295	66	[21]
(Ru-Co)Ox/CC	carbon cloth	10 100	171.2 236.6	-	[12]

Table S5. Comparison of Water Splitting Performance with Recent Reported Electrocatalysts.

Electrocatalyst	Voltage for water splitting at corresponding j (V@mA cm^{-2})	Ref.
IrRuCoNiCu/CC(+)// PtRhCoNiCu/CC(-)	1.51@10 1.61@100 1.76@500 1.88@1000	This work
IrRuCoNiCu/CC	1.52@10 1.64@100 1.84@500	This work
PtRhCoNiCu/CC	1.52@10 1.69@100 1.88@400	This work
AlNiCoRuMo	1.50@10 1.55@20	5
NiCo@C-NiCoMoO/NF	1.71@100 2.01@1000	22
CoMoSx/NF	1.74@100	23
(Ru-Co)Ox/CC	1.488@10 1.568@50 1.617@100	12
RuIrOx	1.47@10 1.54@50	24
RuO_2/NiO/NF	1.5@10 1.58@50	25
Ru/Cu-RuO_2@C	1.47@10 1.57@50 1.67@100	26
NiFeRu-LDH/NF	1.52@10 1.64@50 1.7@100	27

n REFERENCES

(1) Yao, Y.; Huang, Z.; Xie, P.; Lacey, S. D.; Jacob, R. J.; Xie, H.; Chen, F.; Nie, A.; Pu, T.; Rehwoldt, M.; Yu, D.; Zachariah, M. R.; Wang, C.; Shahbazian-Yassar, R.; Li, J.; Hu, L. Carbothermal shock synthesis of high-entropy-alloy nanoparticles. *Science* **2018**, 359, 1489-1494.

(2) Zhang, G.; Ming, K.; Kang, J.; Huang, Q.; Zhang, Z.; Zheng, X.; Bi, X. High entropy alloy as a highly active and stable electrocatalyst for hydrogen evolution reaction. *Electrochim. Acta* **2018**, 279, 19-23.

(3) Liu, M.; Zhang, Z.; Okejiri, F.; Yang, S.; Zhou, S.; Dai, S. Entropy-maximized synthesis of multimetallic nanoparticle catalysts via a ultrasonication-assisted wet chemistry method under ambient conditions. *Adv. Mater. Interfaces* **2019**, 6, 1900015.

(4) Gao, S.; Hao, S.; Huang, Z.; Yuan, Y.; Han, S.; Lei, L.; Zhang, X.; Shahbazian-Yassar, R.; Lu, J. Synthesis of high-entropy alloy nanoparticles on supports by the fast moving bed pyrolysis. *Nat. Commun.* **2020**, 11, 2016.

(5) Jin, Z.; Lyu, J.; Zhao, Y.-L.; Li, H.; Lin, X.; Xie, G.; Liu, X.; Kai, J.-J.; Qiu, H.-J. Rugged high-entropy alloy nanowires with in situ formed surface spinel oxide as highly stable electrocatalyst in Zn-air batteries. *ACS Mater. Lett.* **2020**, 2, 1698-1706.

(6) Wu, D.; Kusada, K.; Yamamoto, T.; Toriyama, T.; Matsumura, S.; Gueye, I.; Seo, O.; Kim, J.; Hiroi, S.; Sakata, O.; Kawaguchi, S.; Kubota, Y.; Kitagawa, H. On the electronic structure and hydrogen evolution reaction activity of platinum group metal-based high-entropy-alloy nanoparticles. *Chem. Sci.* **2020**, 11, 12731-12736.

(7) Yao, R.-Q.; Zhou, Y.-T.; Shi, H.; Wan, W.-B.; Zhang, Q.-H.; Gu, L.; Zhu, Y.-F.; Wen, Z.; Lang, X.-Y.; Jiang, Q. Nanoporous surface high-entropy alloys as highly efficient multisite electrocatalysts for nonacidic hydrogen evolution reaction. *Adv. Funct. Mater.* **2021**, 31, 2009613.

(8) Li, H.; Han, Y.; Zhao, H.; Qi, W.; Zhang, D.; Yu, Y.; Cai, W.; Li, S.; Lai, J.; Huang, B.; Wang, L. Fast site-to-site electron transfer of high-entropy alloy nanocatalyst driving redox electrocatalysis. *Nat. Commun.* **2020**, 11, 5437.

(9) Zhang, D.; Shi, Y.; Zhao, H.; Qi, W.; Chen, X.; Zhan, T.; Li, S.; Yang, B.; Sun, M.; Lai, J.; Huang, B.; Wang, L. The facile oil-phase synthesis of a multi-site synergistic high-entropy alloy to promote the alkaline hydrogen evolution reaction. *J. Mater. Chem. A* **2021**, 9, 889-893.

(10) Jia, Z.; Nomoto, K.; Wang, Q.; Kong, C.; Sun, L.; Zhang, L.-C.; Liang, S.-X.; Lu, J.; Kruzic, J. J. A self-supported high-entropy metallic glass with a nanosponge architecture for efficient hydrogen evolution under alkaline and acidic conditions. *Adv. Funct. Mater.* **2021**, 31, 2101586.

(11) Jia, Z.; Yang, T.; Sun, L.; Zhao, Y.; Li, W.; Luan, J.; Lyu, F.; Zhang, L.-C.; Kruzic, J. J.; Kai, J.-J.; Huang, J. C.; Lu, J.; Liu, C. T. A novel multinary intermetallic as an active electrocatalyst for hydrogen evolution. *Adv. Mater.* **2020**, 32, 2000385.

(12) Wang, C.; Qi, L. Heterostructured inter-doped Ruthenium-cobalt oxide hollow nanosheet arrays for highly efficient overall water splitting. *Angew. Chem. Int. Ed.* **2020**, 59, 17219-17224.

(13) Cui, X.; Zhang, B.; Zeng, C.; Guo, S. Electrocatalytic activity of high-entropy alloys toward oxygen evolution reaction. *MRS Commun.* **2018**, 8, 1230-1235.

(14) Qiu, H.-J.; Fang, G.; Gao, J.; Wen, Y.; Lv, J.; Li, H.; Xie, G.; Liu, X.; Sun, S. Noble metal-free nanoporous high-entropy alloys as highly efficient electrocatalysts for oxygen evolution reaction. *ACS Mater. Lett.* **2019**, 1, 526-533.

(15) Huang, K.; Zhang, B.; Wu, J.; Zhang, T.; Peng, D.; Cao, X.; Zhang, Z.; Li, Z.; Huang, Y. Exploring the impact of atomic lattice deformation on oxygen evolution reactions based on a sub-5 nm pure face-centred cubic high-entropy alloy electrocatalyst. *J. Mater. Chem. A* **2020**, 8, 11938-11947.

(16) Ma, P.; Zhang, S.; Zhang, M.; Gu, J.; Zhang, L.; Sun, Y.; Ji, W.; Fu, Z. Hydroxylated high-entropy alloy as highly efficient catalyst for electrochemical oxygen evolution reaction. *Sci. China Mater.* **2020**, 63, 2613-2619.

(17) Nguyen, T. X.; Liao, Y.-C.; Lin, C.-C.; Su, Y.-H.; Ting, J.-M. Advanced high entropy perovskite oxide electrocatalyst for oxygen evolution reaction. *Adv. Funct. Mater.* **2021**, 31, 2101632.

(18) Nguyen, T. X.; Su, Y.-H.; Lin, C.-C.; Ruan, J.; Ting, J.-M. A new high entropy glycerate for high performance oxygen evolution reaction. *Adv. Sci.* **2021**, 8, 2002446.

(19) Nguyen, T. X.; Su, Y.-H.; Lin, C.-C.; Ting, J.-M. Self-reconstruction of sulfate-containing high entropy sulfide for exceptionally high-performance oxygen evolution reaction electrocatalyst. *Adv. Funct. Mater.* **2021**, 31, 2106229.

(20) Glasscott, M. W.; Pendergast, A. D.; Goines, S.; Bishop, A. R.; Hoang, A. T.; Renault, C.; Dick, J. E. Electrosynthesis of high-entropy metallic glass nanoparticles for designer, multi-functional electrocatalysis. *Nat. Commun.* **2019**, 10, 2650.

(21) Cui, M.; Yang, C.; Li, B.; Dong, Q.; Wu, M.; Hwang, S.; Xie, H.; Wang, X.; Wang, G.; Hu, L. High-entropy metal sulfide nanoparticles promise high-performance oxygen evolution reaction. *Adv. Energy Mater.* **2021**, 11, 2002887.

(22) Qian, G.; Chen, J.; Yu, T.; Luo, L.; Yin, S. N-doped graphene-decorated NiCo alloy coupled with mesoporous NiCoMoO nano-sheet heterojunction for enhanced water electrolysis activity at high current density. *Nano-Micro Lett.* **2021**, 13, 77.

(23) Shan, X.; Liu, J.; Mu, H.; Xiao, Y.; Mei, B.; Liu, W.; Lin, G.; Jiang, Z.; Wen, L.; Jiang, L. An engineered superhydrophilic/superaerophobic electrocatalyst composed of the supported $CoMoS_x$ chalcogel for overall water splitting. *Angew. Chem. Int. Ed.* **2020**, 59, 1659-1665.

(24) Zhuang, Z.; Wang, Y.; Xu, C.-Q.; Liu, S.; Chen, C.; Peng, Q.; Zhuang, Z.; Xiao, H.; Pan, Y.; Lu, S.; Yu, R.; Cheong, W.-C.; Cao, X.; Wu, K.; Sun, K.; Wang, Y.; Wang, D.; Li, J.; Li, Y. Three-dimensional open nano-netcage electrocatalysts for efficient pH-universal overall water splitting. *Nat. Commun.* **2019**, 10, 4875.

(25) Liu, J.; Zheng, Y.; Jiao, Y.; Wang, Z.; Lu, Z.; Vasileff, A.; Qiao, S.-Z. NiO as a bifunctional promoter for RuO_2 toward superior overall water splitting. *Small* **2018**, 14, 1704073.

(26) Yang, K.; Xu, P.; Lin, Z.; Yang, Y.; Jiang, P.; Wang, C.; Liu, S.; Gong, S.; Hu, L.; Chen, Q. Ultrasmall Ru/Cu-doped RuO_2 complex embedded in amorphous carbon skeleton as highly active bifunctional electrocatalysts for overall water splitting. *Small* **2018**, 14, 1803009.

(27) Chen, G.; Wang, T.; Zhang, J.; Liu, P.; Sun, H.; Zhuang, X.; Chen, M.; Feng, X. Accelerated hydrogen evolution kinetics on NiFe-layered double hydroxide electrocatalysts by tailoring water dissociation active sites. *Adv. Mater.* **2018**, 30, 1706279.